COMMUNICATIONS CHEMISTRY

ARTICLE

DOI: 10.1038/s42004-018-0026-y OPEN

Porous amorphous silicon film anodes for high-capacity and stable all-solid-state lithium batteries

Junichi Sakabe[1,5], Narumi Ohta[1,2,3], Tsuyoshi Ohnishi[1,2,3], Kazutaka Mitsuishi[2,4] & Kazunori Takada[1,2,3]

Owing to its high theoretical capacity of ~4200 mAh g^{-1} and low electrode potential (<0.35 V vs. Li^+/Li), utilising silicon as anode material can boost the energy density of rechargeable lithium batteries. Nevertheless, the volume change (~300%) in silicon during lithiation/delithiation makes stable cycling challenging. Since some of the capacity fading mechanisms do not function in solid electrolytes, silicon anodes exhibit better cycling performance in solid electrolytes than liquids. Nonetheless, capacity can fade rapidly because of the difficulties in maintaining mechanical integrity in thick/bulky electrodes, especially when high active material loading is employed to deliver practically useful areal capacity. By contrast, silicon nanostructures can relieve deformation-induced stress and enhance cycling performance. Here we report enhanced cycling performances achieved using nanostructured silicon films and inorganic solid electrolyte and show that amorphous porous silicon films maintain high capacity upon cycling (2962 mAh g^{-1} and 2.19 mAh cm^{-2} after 100 cycles).

[1] Center for Green Research on Energy and Environmental Materials, National Institute for Materials Science, 1-1 Namiki, Tsukuba, Ibaraki 305-0044, Japan. [2] Global Research Center for Environment and Energy Based Nanomaterials Science (GREEN), National Institute for Materials Science, 1-1 Namiki, Tsukuba, Ibaraki 305-0044, Japan. [3] NIMS-TOYOTA Materials Center of Excellence for Sustainable Mobility, National Institute for Materials Science, 1-1 Namiki, Tsukuba, Ibaraki 305-0044, Japan. [4] Research Center for Advanced Measurement and Characterisation, National Institute for Materials Science, 1-2-1 Sengen, Tsukuba, Ibaraki 305-0047, Japan. [5] Present address: Department of Applied Chemistry, Faculty of Science and Engineering, Chuo University, 1-13-27 Kasuga, Bunkyo-ku, Tokyo 112-8551, Japan. Correspondence and requests for materials should be addressed to N.O. (email: ohta.narumi@nims.go.jp)

Silicon has a great potential to boost the energy density of rechargeable Li batteries as an anode material because of its high theoretical capacity (~4200 mAh g^{-1}) and low electrode potential (<0.35 V vs. Li^+/Li)[1]. However, achieving stable cycling is highly challenging due to the extraordinary large volume change (~300%) that Si shows during lithiation/delithiation cycles[2,3]. The large volume change in Si anodes leads to rapid capacity fading through several mechanisms: material pulverisation, morphology change of the entire Si electrode and solid-electrolyte interphase (SEI)[4]. In liquid electrolytes, expansion and shrinkage of Si particles upon charge–discharge cycling causes repetitive exposure of fresh surface, which results in unceasing formation and thickening of SEI layer[5]. By contrast, such SEI layer does not form in solid electrolytes since only Li ions are mobile and any reactants required for SEI are not supplied to the Si surface[6]. Further, morphological changes in solid-state batteries are suppressed since Si anodes are confined to a limited space formed between solid materials—i.e., the current collector and solid electrolyte. Nevertheless, material pulverisation can still cause capacity fading in solid electrolytes.

Previous work has shown that amorphous Si anode films with thickness of up to 0.3 µm display high capacity and good cyclability (for instance, in our previous work[7,8], 1st discharge capacity >3000 mAh g^{-1} and a capacity retention of ~85% after 100 cycles) in solid electrolytes[7–10]. However, the active material loading in the 0.3-µm-thick film provided an areal capacity of 0.2 mAh cm^{-2} only, which is much lower than the values typical for commercial Li-ion batteries (2–4 mAh cm^{-2}). Attempts to increase the areal capacity to practical levels by increasing the thickness was associated with difficulties in maintaining the mechanical integrity[2,3] of electrodes.

Repetitive large volume change upon lithiation/delithiation tends to decrepitate or pulverise Si particles. A recent in situ transmission electron microscopy (TEM) study has revealed that amorphous Si nanospheres with a diameter of up to 870 nm, which is larger than the critical diameter of 150 nm identified for crystalline Si spheres[11], do not fracture[12]. Therefore, the excellent cycling performance of anode films in solid electrolytes can be attributed to their amorphous nature with submicrometre dimensions, as well as morphology confinement and suppression of SEI formation by the solid electrolyte. Nonetheless, the films must be thicker than 3 µm to achieve practical areal capacity of 2 mAh cm^{-2}.

Recently, the critical fracture diameter in liquid electrolytes has further increased to 1.5 µm for porous Si particles[13]. The use of porous materials as electrodes in Li-ion batteries with liquid electrolytes has been studied extensively[13–15]. In such systems, pore walls enlarge the electrode surface area by serving as reaction surfaces when the electrolyte infiltrates the pores. Additionally, the Li diffusion length is reduced to the pore wall thickness. These advantages, however, are not expected in solid-state batteries since solid electrolyte particles do not enter pores. Nevertheless, the porous structures strengthen the structural integrity of the anode and might thus enhance the cycling stability of Si films in solid electrolytes with sufficient thickness for practical applications.

Herein, we address capacity fading by combining nanostructured Si films with inorganic solid electrolyte. In the solid electrolyte, amorphous Si films with porous structure deliver excellent cyclability (2962 mAh g^{-1} and 2.19 mAh cm^{-2} after 100 cycles).

Results

Characterisation of amorphous Si films. Figure 1 shows representative surface and cross-sectional morphologies of non-porous and porous amorphous Si films prepared in this study. Both types of films were prepared by magnetron sputtering. The non-porous films were prepared using conventional Ar gas, which produced dense films (Fig. 1e, f, i, j) with a density of 2.3 g cm^{-3}, which is comparable to the theoretical value of crystalline Si (2.33 g cm^{-3}). The surfaces of these films were homogeneous and essentially flat (Fig. 1a, b). By contrast, He was used as the sputtering gas for the preparation of porous films; according to the previous studies[16,17], it is known that He can be incorporated in the amorphous Si films during deposition and thus He bubbles are formed due to the extremely low solubility of He in metals. The resulting films exhibited (Fig. 1g, h, k, l and Supplementary Fig. 1a, c) homogeneously distributed pores, ranging from 10 to 50 nm in size, separated by 10-nm-thick walls. The density of the obtained films was ~1.5 g cm^{-3}. Assuming the porous structure of the films consists of pores and walls of dense amorphous Si, the porosity is about 40%. The porous films had uneven surface with a number of mountain-like projections with an average lateral size of 100 to 200 nm and height of <50 nm (Fig. 1c, d). The amorphous nature of the non-porous and porous Si films was confirmed by grazing incidence X-ray diffraction (GIXRD) and Raman spectroscopy, which demonstrated that all the films prepared in this study were amorphous without inclusion of crystalline Si (Supplementary Figs. 2 and 3).

Cycling properties. The capacities of non-porous and porous film anodes observed in the 1st cycles are listed in Supplementary Tables 1 and 2, respectively. Figures 2a, b and 3a, b show the potential profiles of the prepared Si films during the first five charging/discharging cycles in a thiophosphate-based solid electrolyte ($80Li_2S{\cdot}20P_2S_5$ glass). The profiles of the porous Si films (Figs. 2b and 3b) are almost identical to those of the non-porous films (Figs. 2a and 3a) as well as to those of previously reported 0.3-µm-thick amorphous Si films in a thiophosphate-based solid electrolyte[7,8]. These results indicate that the amorphous Si phase, which forms the pore walls, is, indeed, responsible for the electrode reaction. By contrast, remarkable differences were found in the cycling performance of the non-porous and porous films—the porous structure improved the performance dramatically.

As revealed by in situ TEM observation of lithiation of amorphous Si nanospheres, amorphous spheres with diameter up to 870 nm do not fracture[12]. The thickness of films examined in this study (1 and 3 µm for non-porous films) exceeds this critical value, and thus the non-porous films show capacity fading, which is accelerated by increasing thickness. After 100 cycles, the 3-µm-thick film showed only ~47% of its capacity at the 10th cycle, while the capacity was retained ~82% for the 1-µm-thick film. These results show that while capacity fading in thin films with thickness slightly above the limit is moderate, it increases considerably together with increasing thickness. The fracture or decrepitation causes breaks in the pathways for Li-ion and electron conductions, thereby increasing electrode resistance during cycling and causing capacity fading. For the 1- and 3-µm-thick non-porous films, gradual and rapid increases in electrode resistance during cycling, respectively, were identified in the relevant differential capacity curves (Figs. 2d and 3d). As the cycling proceeds, the positions of the charging and discharging peaks move towards more negative and positive potentials, respectively. Correspondingly, the peak currents decrease with cycling. In contrast to non-porous films, the porous films exhibited excellent cycling stabilities—both films delivered high capacities of ~3000 mAh g^{-1} and showed more than 93% retention of their respective 10th cycle's capacities after 100 cycles and high Coulombic efficiencies exceeding 99.8% (Figs. 2c and 3c). In addition, the positions of all peaks in the

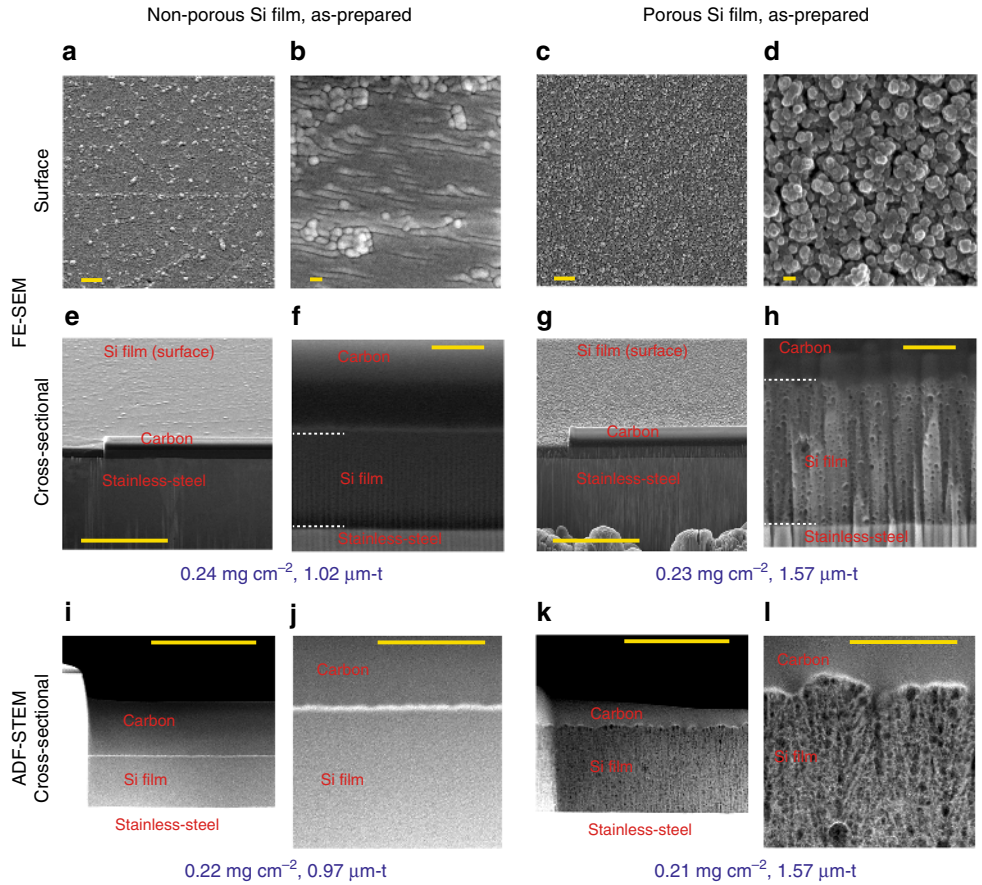

Fig. 1 Microscopy images of as-prepared amorphous Si films. **a**–**d** Field-emission scanning electron microscopy (FE-SEM) images of surface of **a**, **b** non-porous and **c**, **d** porous films. The scale bar for (**a**, **c**) represents 1 μm. The scale bar for (**b**, **d**) represents 100 nm. **e**–**h** FE-SEM cross-sectional images of **e**, **f** non-porous and **g**, **h** porous films. The cross-sectional FE-SEM images were obtained at a tilt angle of 60°, and thus the scale bars in the images are only applicable to the horizontal direction. The upper and lower dashed white lines in (**f**) and (**h**) indicate the surfaces of amorphous Si films and stainless-steel substrates, respectively. The scale bar for (**e**, **g**) represents 10 μm. The scale bar for (**f**, **h**) represents 500 nm. **i**–**l** Annular dark-field scanning transmission electron microscopy (ADF-STEM) cross-sectional images of **i**, **j** non-porous and **k**, **l** porous films. The scale bar for (**i**, **k**) represents 2 μm. The scale bar for (**j**, **l**) represents 500 nm. The microscopy images acquired using higher magnifications for the low-magnification images of (**a**), (**c**), (**e**), (**g**), (**i**) and (**k**) are presented in (**b**), (**d**), (**f**), (**h**) and (**j**), respectively. The non-porous and porous Si films were prepared by magnetron sputtering with Ar at 0.4 Pa and He at 5 Pa, respectively. The carbon top layers onto the Si films in the cross-sectional images are protection layers against damage from focused ion beam (FIB). The areal mass loadings and the thicknesses of the observed films are indicated below the corresponding images; the surface and cross-sectional FE-SEM images were taken from the same samples and the values are indicated below the cross-sectional images

differential capacity plots remained virtually unchanged for the porous films (Figs. 2e and 3e), suggesting structural stability during cycling.

Electrochemical impedance spectra measured after the cycling performance tests (Fig. 4) revealed that the increase of electrode impedance was remarkable for the non-porous and thick film that showed the fast capacity fading indeed. The non-porous and porous films did not show noticeable differences between their impedance spectra after the cycling, when the areal capacity was ~0.6 mAh cm^{-2}, as shown in Fig. 4a, b. On the other hand, clear differences in the impedance spectra were observed between the non-porous and porous films with the areal capacity of ~2 mAh cm^{-2}. Each spectrum in Fig. 4c, d consists of a straight line in the low-frequency region (<10^{-1} Hz) and an arc in the middle-frequency region (10^{3}–10^{-1} Hz), which can be attributed to diffusion and charge transfer resistances, respectively. They are higher in the non-porous film than in the porous one, which suggests the capacity fading in the thicker non-porous film caused by both lowering the Li-ion diffusivity and increasing interfacial charge transfer resistance of the film.

The cycled films taken out from the cells were observed under an electron microscope in order to identify morphological changes in the cycled anodes that cause the significant differences in cycling stability between the thicker films. The pores remained in the porous film with slightly expanded diameters after 100 cycles (Supplementary Fig. 1b, d), and the density and width of the through-thickness cracks in the cycled non-porous film were higher and wider, respectively, than those for the cycled porous film (Supplementary Fig. 4). The narrower cracks with lower density for the porous film suggest that the pores suppress the changes in the outer shape by accommodating volume expansion to maintain the contact to the solid electrolyte and minimise the increase in the resistance.

Figure 5 compares the cross-sectional images of fully charged non-porous and porous films with areal mass loading of 0.23 mg cm^{-2}. It should be noted that, although the thickness of the films was increased compared to the as-prepared ones, the charged films showed homogeneous thicknesses and thus planar surfaces. After the 6th charging with a capacity of 2880 mAh g^{-1} (Supplementary Fig. 5a), the thickness of the non-porous film

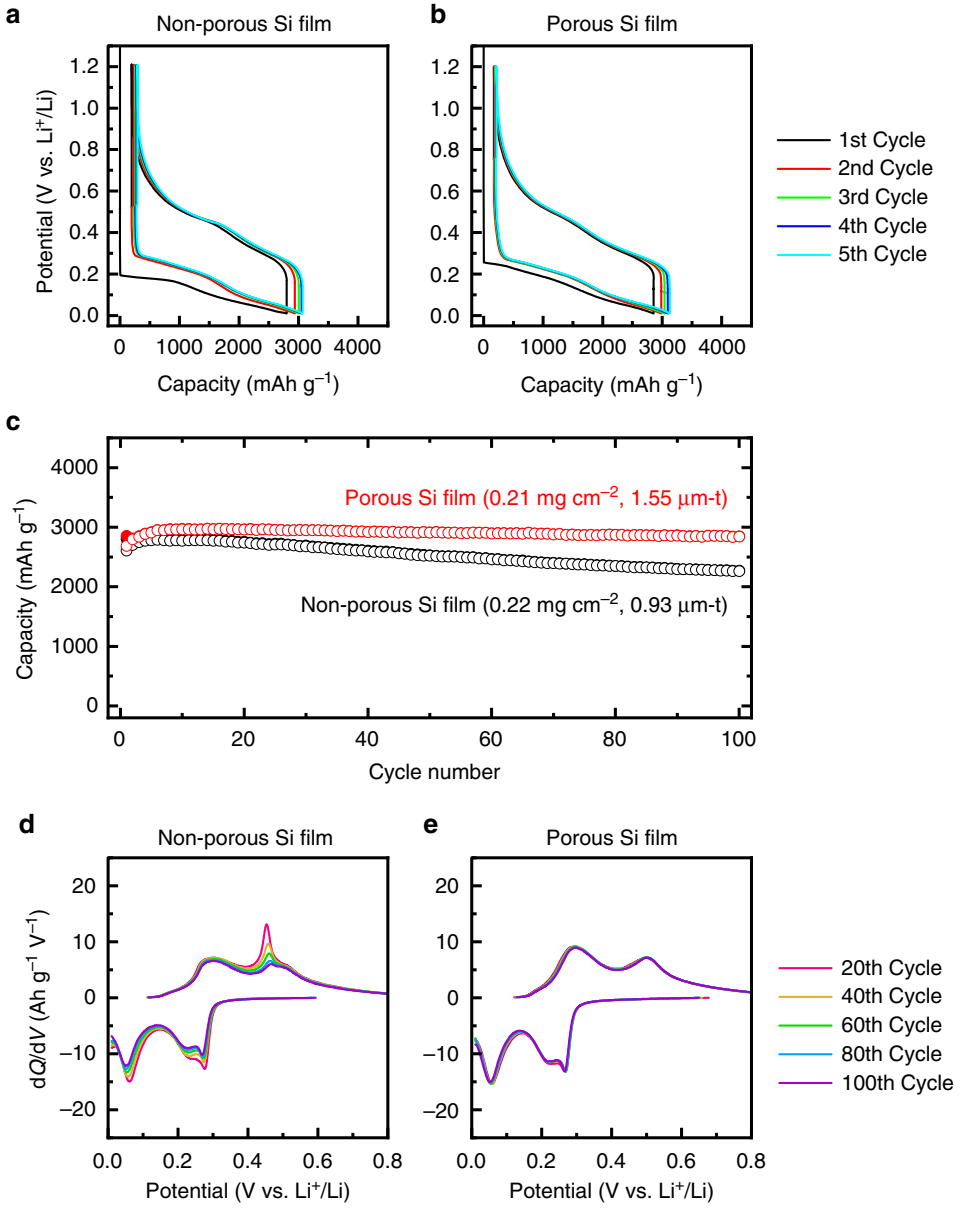

Fig. 2 Cycling performances of amorphous Si films. The films show areal capacities of ~0.6 mAh cm^{-2} at a current density of 0.1 mA cm^{-2}. **a**, **b** Galvanostatic charging/discharging potential profiles of **a** non-porous and **b** porous Si films during the first five cycles: the black, red, green, blue and cyan curves indicate the profiles in the 1st, 2nd, 3rd, 4th and 5th cycles, respectively. **c** Charging/discharging capacities plotted against the cycle number. The filled and empty circles indicate the charging and discharging capacities, respectively; the black and red circles represent the results for non-porous and porous Si films, respectively. **d**, **e** Differential capacity curves for **d** non-porous and **e** porous Si films: the red, orange, green, light blue and purple curves indicate those in the 20th, 40th, 60th, 80th and 100th cycles, respectively. The curves were calculated from the corresponding galvanostatic charging/discharging potential profiles of the films. The areal mass loadings of the as-prepared non-porous and porous films were 0.22 and 0.21 mg cm^{-2}, respectively, and the thicknesses were 0.93 and 1.55 µm, respectively

reached 3.0 µm (Fig. 5a, c, e). The observed increase in thickness (2.0 µm) in the non-porous film agrees well with the change expected based on the volume expansion observed in liquid electrolytes[18] and charge capacity. By contrast, thickness of the porous anode film increased to 3.4 µm (Fig. 5b, d, f) at a charge capacity of 3279 mAh g^{-1} (Supplementary Fig. 5b). Again, this thickness agrees with that expected from the relationship between volume expansion and charge capacity[18]—the mass loading of 0.23 mg cm^{-2} corresponds to the thickness of 1.0 µm in the dense film, which should expand to a 3.3-µm-thick film at 3279 mAh g^{-1} charge (see Supplementary Tables 3 and 4). These outcomes suggest that the pores accommodate volume expansion upon charging. In fact, the fully charged film displayed reduced number and size of pores (see the inset of Fig. 5f). It should be noted however that the pore volume is insufficient to accommodate the expansion completely—pores at film density of 1.5 g cm^{-3} cover only ~20% of the expansion. Based on the volume expansion observed in Fig. 5, the porous films with areal capacities of 0.6 and 2 mAh cm^{-2} (Figs. 2 and 3) should undergo extraordinarily large increases in thickness of 1.2 and 5.9 µm, respectively, during lithiation (Supplementary Table 4). The cycling stabilities observed for the porous anode films in spite of insufficient pore

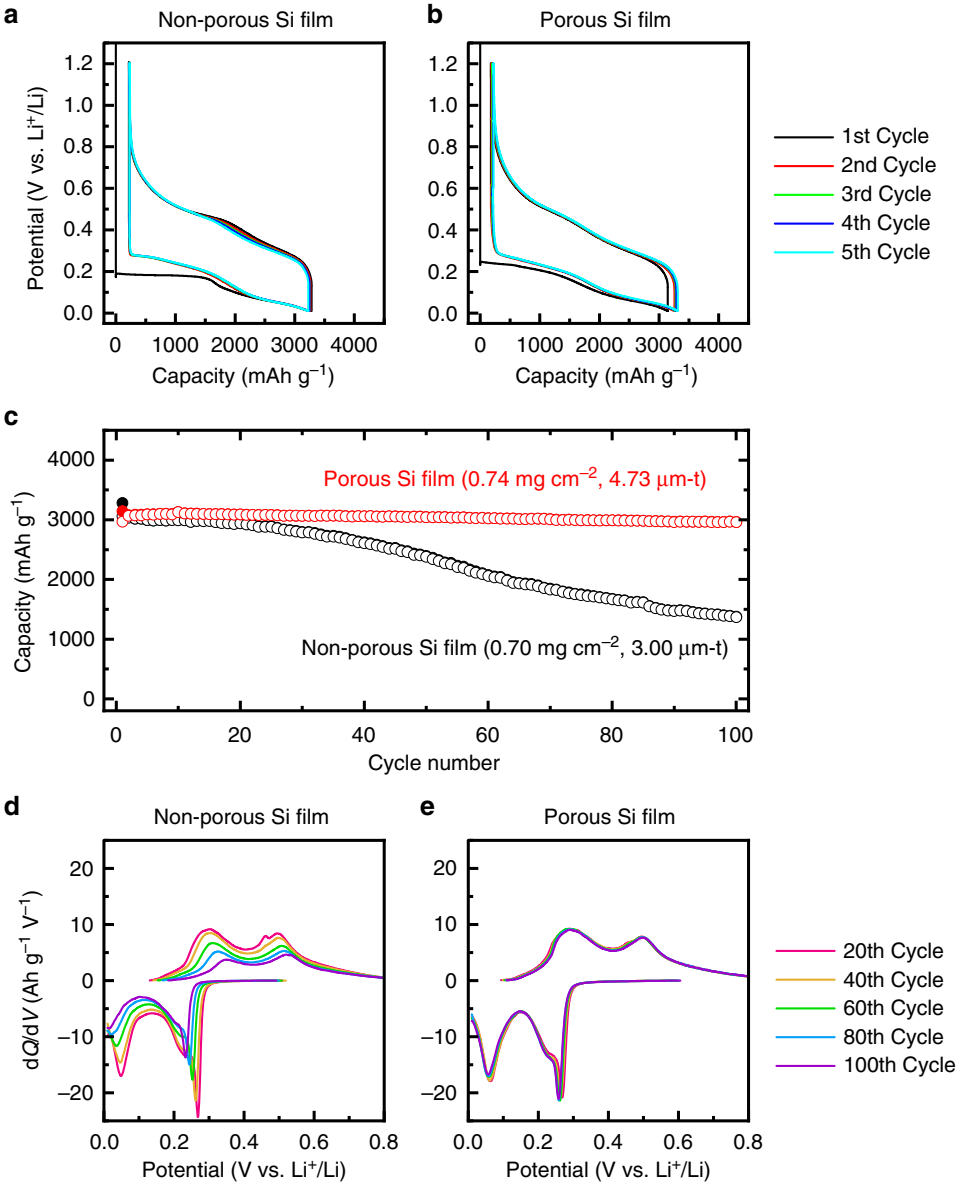

Fig. 3 Cycling performances of amorphous Si anode films. The films show areal capacities of ~2 mAh cm^{-2} at a current density of 0.1 mA cm^{-2}. **a**, **b** Galvanostatic charging/discharging potential profiles of **a** non-porous and **b** porous Si films during the first five cycles: the black, red, green, blue and cyan curves indicate the profiles in the 1st, 2nd, 3rd, 4th and 5th cycles, respectively. **c** Charging/discharging capacities plotted against the cycle number. The filled and empty circles indicate the charging and discharging capacities, respectively; the black and red circles represent the results for non-porous and porous Si films, respectively. **d**, **e** Differential capacity curves for **d** non-porous and **e** porous Si films: the red, orange, green, light blue and purple curves indicate those in the 20th, 40th, 60th, 80th and 100th cycles, respectively. The curves were calculated from the corresponding galvanostatic charging/discharging potential profiles of the films. The areal mass loadings of the as-prepared non-porous and porous films were 0.70 and 0.74 mg cm^{-2}, respectively, and the thicknesses were 3.00 and 4.73 µm, respectively

volume suggest that the mechanical properties of the solid electrolyte also play an important role in circumventing the structural deterioration of the interface in terms of Li-ion transfer.

The volume changes appear as the changes in film thickness in this study because of the extremely large ratios of surface area to volume in thin films. The thiophosphate-based solid electrolyte used in this study, $80Li_2S{\cdot}20P_2S_5$ glass, exhibits a relatively low elastic modulus (~20 GPa) and deforms readily by compression at high pressure[19]. These mechanical properties will contribute to maintaining the anode/electrolyte interface against the quasi-one-dimensional volume change of anodes, which is partially reduced by introduction of pores, under uniaxial pressure applied perpendicular to the film surface.

High-rate properties. Finally, the influence of pores on the rate capability must be discussed. Rate capability is usually enhanced in porous materials when combined with liquid electrolytes because filling of the pores with liquid electrolyte enlarges the electrode surface and shortens the Li diffusion length. By contrast, solid electrolytes never enter the pores and thus the porous structure could worsen the rate capability of a solid system since Li has to diffuse through very thin pore walls (10 nm thickness in the delithiated state) for electrode reactions.

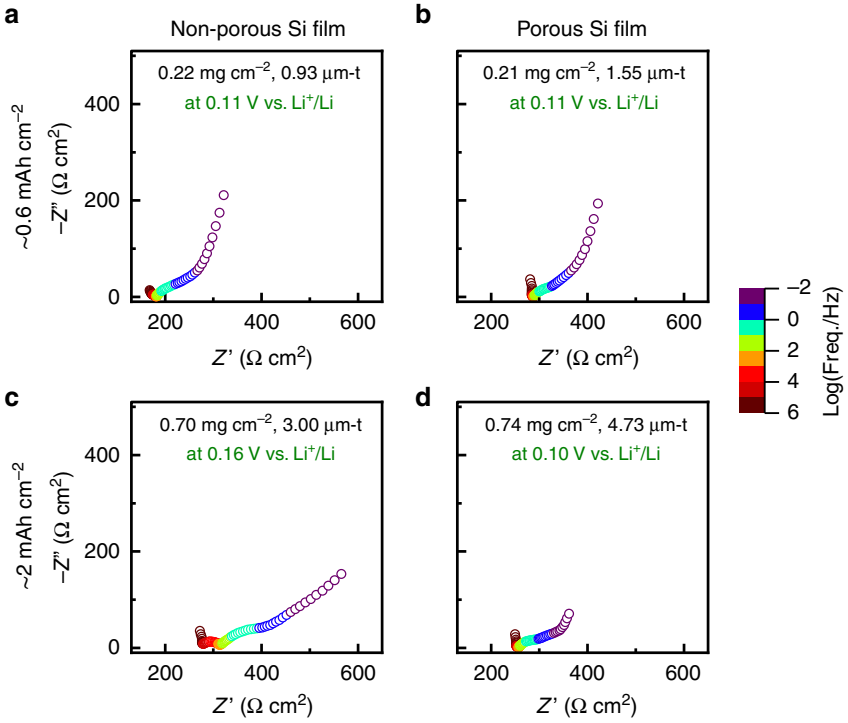

Fig. 4 Electrochemical impedance spectra of amorphous Si films measured after 101st film charging. **a**, **b** Electrochemical impedance spectra of **a** non-porous and **b** porous Si films showing areal capacity of ~0.6 mAh cm^{-2}. **c**, **d** Electrochemical impedance spectra of **c** non-porous and **d** porous Si films showing areal capacity of ~2 mAh cm^{-2}. The films were cycled with a current density of 0.1 mA cm^{-2} in the potential range of 0.01–1.2 V vs. Li$^+$/Li, whose cycling performances over the first 100 cycles are shown in Figs. 2 and 3. The colour scale bar shown on the right side of the figure represents the frequency of the applied AC perturbation signal. The spectra were obtained at open-circuit voltages indicated in the corresponding panels after 5 h of rest. The areal mass loadings and thicknesses of the as-prepared films are also indicated in the corresponding panels

Figure 6 compares the discharging rate capabilities of the non-porous and porous films. Amorphous Si films exhibited very high-rate capability, i.e., very small activation and diffusion overvoltages[7,8], and thus the resistance overvoltage in the electrolyte layer is the dominant factor in the polarisation observed for the solid-state electrochemical cells in this study. Therefore, discharge curves shown in Fig. 6 were obtained by excluding the polarisation originating from the electrolyte layer resistance (Supplementary Figs. 6 and 7) to compare the rate capabilities inherent in the films. The results clearly show that the discharge curves of the porous and non-porous films are almost identical, demonstrating that the introduction of pores has no detrimental effect on the rate capability. The thinner films maintained discharge capacities >3000 mAh g^{-1}, even at 10 mA cm^{-2} (17 C), and the thicker films delivered an extraordinary high areal capacity of >2 mAh cm^{-2} at current density of 2 mA cm^{-2}. Even at higher current density of 10 mA cm^{-2} (discharge rate of 3 C), the films showed discharge capacities higher than 1700 mAh g^{-1} and 1.2 mAh cm^{-2}. These results confirm that the high rate capability of amorphous Si in solid electrolytes is retained in the porous form.

Discussion

In conclusion, the porous character of amorphous Si enhances cycling performance in solid electrolytes without lowering their high specific capacity or high rate capability. The porous structure is thought to strengthen the structural integrity of the electrode through inherent rapid stress relaxation capability and by accommodating the expanded volume into the pores. Although similar improved cyclability has been reported for nanostructured Si[20], it should be emphasised that the improvement was achieved at electrode dimensions showing high areal capacities exceeding 2 mAh cm^{-2}. Anodes consisting of nanostructured Si often have large open space and small active material loading, which lower the volumetric and areal capacities to impractical values. By contrast, a porous film that exhibits a very low capacity fading rate of 0.06% per cycle even at a high areal mass loading of 0.7 mg cm^{-2} to deliver a practical areal capacity of 2.3 mAh cm^{-2} and its gravimetric capacity of 3128 mAh g^{-1} corresponds to a high volumetric capacity of 1900 mAh cm^{-3}.

Solid-state batteries have been regarded as critical to addressing the safety issues in Li-ion batteries. Although they had been suffering from low power densities, they have become more powerful than conventional liquid electrolyte systems through the development of solid electrolytes with Li-ion conductivities superior to those of conventional organic liquid electrolytes employed in commercial Li-ion batteries[21]. This study has demonstrated that amorphous Si exhibits higher performance in terms of energy and power densities with excellent cycling durability in solid electrolytes. These properties may impart enhanced energy densities to solid-state batteries, thus corroborating all-solid-state Li batteries as candidates for next-generation high-performance batteries.

Methods

Preparation and characterisation of amorphous Si films. Amorphous Si films were deposited by radio-frequency magnetron sputtering (SPAD-2240UM, Advanced Optics Vacuum Co., Ltd) from a 5N-pure Si target (Kojundo Chemical Laboratory Co., Ltd) at glancing angle geometry with an angle of 30° between the target and substrate normal, keeping the substrate bias at 5 V and the substrate temperature at 100 °C. The distance between the substrate and target was 15 cm.

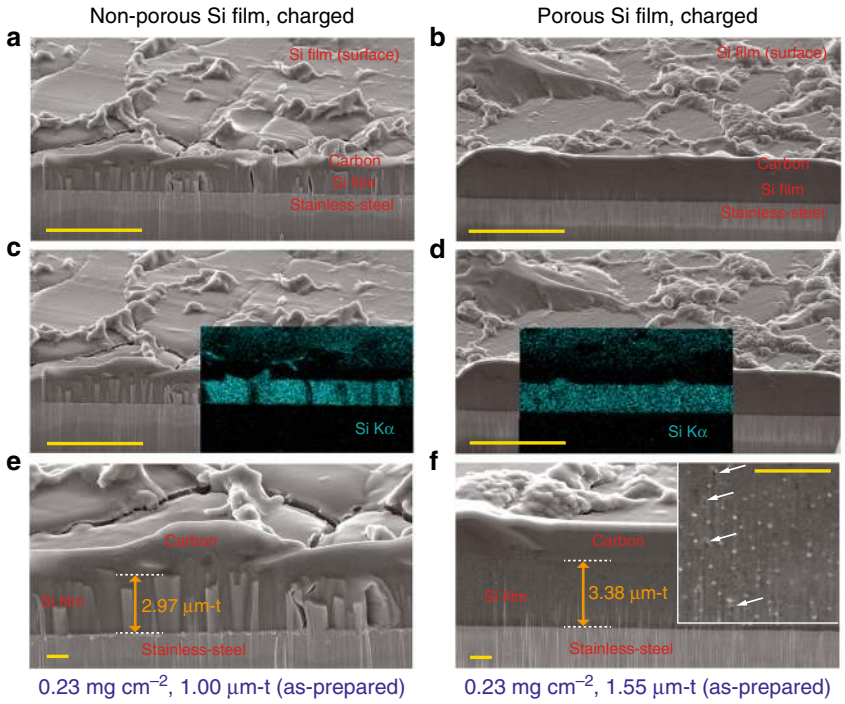

Fig. 5 Microscopy images of fully charged amorphous Si anode films. **a**–**d** FE-SEM cross-sectional images of **a**, **c** non-porous and **b**, **d** porous films. Scale bars represent 10 μm. In order to clarify the anode films' cross-sections, EDS elemental mapping images for Si are overlaid on the corresponding FE-SEM images in (**c**) and (**d**). **e**, **f** High-magnification images of **e** non-porous and **f** porous films. Scale bars represent 1 μm. The cross-sectional FE-SEM images were taken at a tilt angle of 60°, and thus the scale bar in the images is only applicable to the horizontal direction. The upper and lower dashed white lines in (**e**) and (**f**) indicate the surfaces of amorphous Si films and stainless-steel substrates, respectively. The carbon top layers onto the Si films in the figures are protection layers against damage from FIB. Inset in (**f**) shows higher-magnification image and the white arrows in the inset indicate representative shrunk pores in the fully charged porous Si film. The areal mass loadings of the as-prepared non-porous and porous films were 0.23 mg cm^{-2}, and the thicknesses of these films were 1.00 and 1.55 μm, respectively. The anode films were cycled with a current density of 0.1 mA cm^{-2} in the voltage range of 0.01–1.2 V vs. Li^+/Li (see Supplementary Fig. 5 for galvanostatic charging/discharging potential profiles of the anode films) and subsequently the solid-state electrochemical cells were disassembled at lithiated state after 6th charging in an Ar-filled glove box. The thicknesses of the fully charged non-porous and porous films were 2.97 and 3.38 μm, respectively

The substrates were 10-mm-diameter stainless-steel disks that were polished by 4000-grit sandpaper, cleaned by ultrasonic treatment in acetone (99.5% purity, Wako Pure Chemical Industries, Ltd) and annealed in vacuum at 800 °C before deposition. To eliminate loss of the active material deposited on the side of the substrate disks, the Si films were deposited through a mask with an opening diameter of 8.5 mm. The base pressure before sputtering was below 10^{-5} Pa and the radio-frequency power was fixed at 200 W. The thickness of the obtained films was measured using a surface profiler (Dektak 150, Veeco Instruments Inc.). The weight of the films was measured using an electric microbalance (XP6U, Mettler-Toledo Inc.).

The surface and cross-sectional morphologies of the obtained films were observed using a field-emission scanning electron microscope (JSM-7800F, JEOL Ltd) and a scanning transmission electron microscope (JEM-ARM200F, JEOL Ltd). The specimens were prepared using a multi-beam processing system (JIB-4501, JEOL Ltd) incorporating a thermoionic scanning electron microscope and a focused ion beam (FIB) milling after depositing a protective carbon layer.

To characterise the crystallinity of the obtained films, GIXRD measurements were conducted on a diffractometer (SmartLab, Rigaku Corp.) using Cu Kα as the radiation source at operating voltage of 45 kV in parallel beam mode. The grazing angle of the incident X-rays relative to the sample surface was 0.25°; diffraction data were collected in the two theta (2θ) range from 3° to 90°. The local structure of the obtained films was further examined by Raman scattering spectra on a laser Raman microscope (RAMANtouch VIS-NIR, Nanophoton) with excitation at 532 nm in the x-line mode of operation. The laser beam was shaped into a line by a cylindrical lens and focused onto the sample surface by an objective lens with a 50× magnification and a numerical aperture of 0.70. The laser power at the sample was 100 μW. Backward Raman scattering signals from the illuminated line were collected through the same objective lens and sent into a high-resolution spectrometer through a 70-μm-wide entrance slit. All Raman scattering spectra were obtained as averages of eight spectra with an integration time of 15 s. Wavenumbers were calibrated by reference to the emission lines of Ne.

Cell fabrication and electrochemical measurements. A thiophosphate-based solid electrolyte, $80Li_2S{\cdot}20P_2S_5$ glass, was used for the electrochemical measurements, which was synthesised by mechanical milling as reported in literature[11] with minor modifications. Crystalline powders of Li_2S (99% purity, Furukawa Co., Ltd) and P_2S_5 (99% purity, Sigma-Aldrich Co. LLC) were manually mixed in a 4:1 molar ratio using an agate mortar and pestle. The mixture (2 g) was put into a zirconium oxide pot with 45 ml inner volume along with zirconium oxide balls (5 mm diameter) at a powder-to-ball ratio of 1:16. The pot was sealed under an Ar atmosphere and high-energy ball-milling was performed at 25 °C using a planetary micro mill (Pulverisette 7 classic line, Fritsch GmbH). The following milling conditions were employed: 99 alternations of 12 min milling at 500 rpm with 6 min interval in between.

All-solid-state cells were assembled with the $80Li_2S{\cdot}20P_2S_5$ glass as the solid electrolyte and an In-Li alloy, showing a potential plateau at 0.62 V vs. Li^+/Li, as the counter electrode. 100 mg of the solid electrolyte powder was pressed into a pellet with 10-mm diameter at ~360 MPa; although ~1 mm of the resultant thickness of the pellet was thick and led to relatively high electrolyte layer resistance of ~150 Ω cm^{-2}, we chose the weight to minimise the possibility that the capacity fading of the anode films measured originates from the mechanical function of the electrolyte layer. The amorphous Si film was attached to one side of the electrolyte pellet as the working electrode. The counter electrode was formed on the other side by attaching 10-mm-diameter disks of Li metal (~2 mg) and In metal (~60 mg), which were hole-punched from a Li metal foil (50 μm thick, Honjo Chemical Corp.) and an In metal foil (100 μm thick, Rare Metallic Co., Ltd), respectively. The disks were pressed together at ~120 MPa by tightening bolts of a lab-made battery cell[22] into a three-layered pellet that acted as a two-electrode cell. It should be noted that porous structures formed in the obtained films can withstand the pressure applied during the cell assembly (see Supplementary Fig. 8a, b for scanning electron microscopy (SEM) cross-sectional images of the film measured before and after cell assembly, respectively). The cells were constructed in an Ar-filled glove box where O_2 and water concentrations were kept below the level of several ppm.

The cycling performance of the amorphous Si film electrodes in an all-solid-state cell was evaluated by galvanostatic charging/discharging cycling with a constant current density of 0.1 mA cm^{-2} and a rest period of 1 h. A multichannel potentiostat/galvanostat (PS-08, Toho Technical Research Co., Ltd) was used and

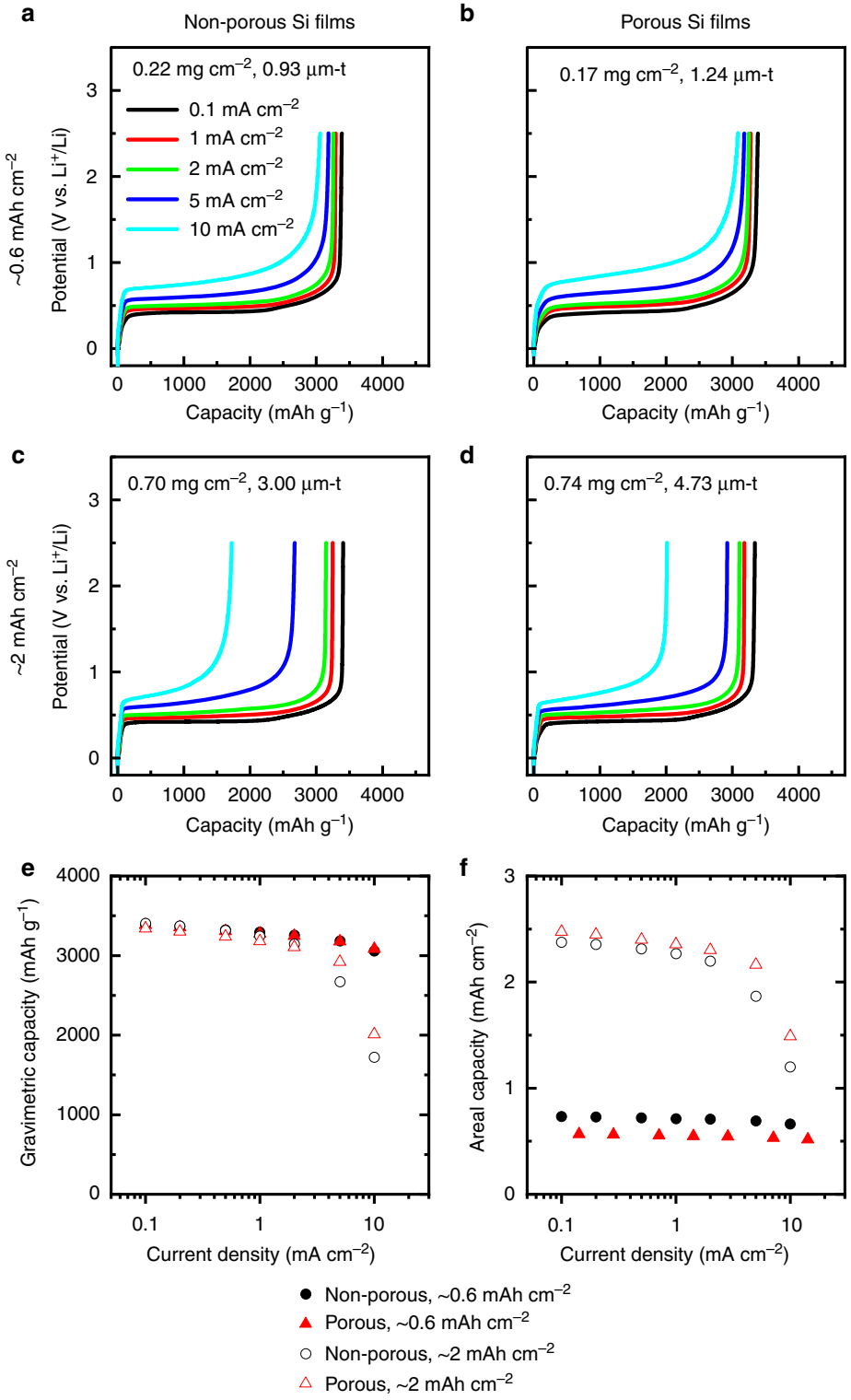

Fig. 6 Discharging rate capabilities of amorphous Si anode films. **a**–**d** Results of rate capability tests for **a** non-porous and **b** porous films showing areal capacity of ~0.6 mAh cm^{-2} and **c** non-porous and **d** porous films showing areal capacity of ~2 mAh cm^{-2} at a current density of 0.1 mA cm^{-2} to 10 mA cm^{-2}. The black, red, green, blue and cyan curves indicate the discharging curves at a constant current of 0.1, 1, 2, 5 and 10 mA cm^{-2}, respectively. In order to facilitate comparison of the rate capabilities of the films, the individual curves were shifted along the potential axis by subtracting the polarisations resulting from the resistances of electrolyte layer; the raw data for the rate capabilities are shown in Supplementary Fig. 4; the electrochemical impedance spectra shown in Supplementary Fig. 5 were used to determine the resistances of the electrolyte layers. The areal mass loadings and the thicknesses of the films used are indicated in the corresponding panels. **e** Observed discharging gravimetric capacities plotted against current densities. **f** Observed discharging areal capacities plotted against current densities. The black filled and empty circles in (**e**) and (**f**) indicate the results for non-porous films with an areal capacity of ~0.6 and ~2 mAh cm^{-2}, respectively; the red filled and empty triangles in (**e**) and (**f**) indicate results for porous films with an areal capacity of ~0.6 and ~2 mAh cm^{-2}, respectively

the lower and upper cut-off voltages were set at −0.61 V and 0.58 V, respectively, in order to cycle the working electrode in the potential range of 0.01–1.2 V vs. Li^+/Li. The discharging rate capability was evaluated at current densities ranging from 0.1 to 10 mA cm^{-2} using a multichannel potentiostat/galvanostat equipped with frequency response analysers (VMP300, Bio-Logic Science Instruments SAS). Prior to discharging, the film anode was charged at a constant current density of 0.1 mA cm^{-2} to 0.01 V vs. Li^+/Li and kept at that potential until the current density decreased to 1 μA cm^{-2} (CC–CV mode). Prior to the rate capability measurements, the electrochemical impedance spectroscopy was performed at an open-circuit potential in order to measure the electrolyte resistance and determine the upper cut-off voltages for discharging. Impedance spectra were taken in the charged state in the frequency range from 1 MHz to 10 mHz with the AC perturbation signal of 10 mV. All electrochemical measurements were conducted at 25 °C.

Note that the voltages in this paper are presented by adding the potential of the In-Li alloy (0.62 V vs. Li^+/Li) to the actually measured cell voltage to show the data as if Li metal was used as the counter electrode. It should also be noted that electrochemical lithiation, or alloying of Si with Li, is expressed as charging in this paper, whereas discharging represents delithiation or dealloying since this paper reports the electrode properties of amorphous Si as an anode.

Data availability. The data supporting the findings of this study are available within the article and its Supplementary Information files. All other relevant source data are available from the corresponding author upon reasonable request.

Received: 20 October 2017 Accepted: 30 March 2018
Published online: 03 May 2018

References

1. Huggins, R. A. Lithium alloy negative electrodes. *J. Power Sources* **81**, 13–19 (1999).
2. Liang, B., Liu, Y. & Xu, Y. Silicon-based materials as high capacity anodes for next generation lithium ion batteries. *J. Power Sources* **267**, 469–490 (2014).
3. Ma, D., Cao, Z. & Hu, A. Si-based anode materials for Li-ion batteries: a mini review. *Nano-Micro Lett.* **6**, 347–358 (2014).
4. Wu, H. & Cui, Y. Designing nanostructured Si anodes for high energy lithium ion batteries. *Nano Today* **7**, 414–429 (2012).
5. Wu, H. et al. Stable cycling of double-walled silicon nanotube battery anodes through solid-electrolyte interphase control. *Nat. Nanotechnol.* **7**, 310–315 (2012).
6. Hayashi, A. et al. Characterization of Li_2S-P_2S_5 glass-ceramics as a solid electrolyte for lithium secondary batteries. *Solid State Ion.* **175**, 683–686 (2004).
7. Miyazaki, R., Ohta, N., Ohnishi, T., Sakaguchi, I. & Takada, K. An amorphous Si film anode for all-solid-state lithium batteries. *J. Power Sources* **272**, 541–545 (2014).
8. Miyazaki, R., Ohta, N., Ohnishi, T. & Takada, K. Anode properties of silicon-rich amorphous silicon suboxide films in all-solid-state lithium batteries. *J. Power Sources* **329**, 41–49 (2016).
9. Phan, V. P., Pecquenard, B. & Le Cras, F. High-performance all-solid-state cells fabricated with silicon electrodes. *Adv. Funct. Mater.* **22**, 2580–2584 (2012).
10. Cervera, R. B. et al. High performance silicon-based anodes in solid-state lithium batteries. *Energy Environ. Sci.* **7**, 662–666 (2014).
11. Liu, X. H. et al. Size-dependent fracture of silicon nanoparticles during lithiation. *ACS Nano* **6**, 1522–1531 (2012).
12. McDowell, M. T. et al. In situ TEM of two-phase lithiation of amorphous silicon nanospheres. *Nano Lett.* **13**, 758–764 (2013).
13. Shen, C. F. et al. In situ and ex situ TEM study of lithiation behaviours of porous silicon nanostructures. *Sci. Rep.* **6**, 31334 (2016).
14. Kim, H., Han, B., Choo, J. & Cho, J. Three-dimensional porous silicon particles for use in high-performance lithium secondary batteries. *Angew. Chem. Int. Ed.* **47**, 10151–10154 (2008).
15. Cheng, H. et al. Periodic porous silicon thin films with interconnected channels as durable anode materials for lithium ion batteries. *Mater. Chem. Phys.* **144**, 25–30 (2014).
16. Godinho, V. et al. A new bottom-up methodology to produce silicon layers with a closed porosity nanostructure and reduced refractive index. *Nanotechnology* **24**, 275604 (2013).
17. Schierholz, R. et al. STEM–EELS analysis reveals stable high-density He in nanopores of amorphous silicon coatings deposited by magnetron sputtering. *Nanotechnology* **26**, 075703 (2015).
18. He, Y. et al. Shape evolution of patterned amorphous and polycrystalline silicon microarray thin film electrodes caused by lithium insertion and extraction. *J. Power Sources* **216**, 131–138 (2012).
19. Sakuda, A., Hayashi, A. & Tatsumisago, M. Sulfide solid electrolyte with favorable mechanical property for all-solid-state lithium battery. *Sci. Rep.* **3**, 2261 (2013).
20. Szczech, J. R. & Jin, S. Nanostructured silicon for high capacity lithium battery anodes. *Energy Environ. Sci.* **4**, 56–72 (2011).
21. Kato, Y. et al. High-power all-solid-state batteries using sulfide superionic conductors. *Nat. Energy* **1**, 16030 (2016).
22. Seino, Y. et al. Synthesis of phosphorous sulfide solid electrolyte and all-solid-state lithium batteries with graphite electrode. *Solid State Ion.* **176**, 2389–2393 (2005).

Acknowledgements

We acknowledge the financial support provided by the New Energy and Industrial Technology Development Organization (NEDO), Japan, and the Toyota Motor Corporation for a project entitled "Applied and Practical LiB Development for Automobile and Multiple Applications." We thank M. Ishikawa and A. Takata for preparing the solid electrolyte. We also thank K. Shinoda and M. Oshida for technical support regarding FE-SEM observations and FIB milling.

Author contributions

N.O. and K.T. conceived the experiments. N.O., T.O. and K.T. coordinated and guided the project. K.M. performed the STEM observations and T.O. performed the GIXRD measurements. J.S. performed all other experiments. All authors analysed the data and contributed to project discussions. J.S., N.O. and K.T. prepared the manuscript with revisions from other authors.

Additional information

Supplementary information accompanies this paper at https://doi.org/10.1038/s42004-018-0026-y.

Competing interests: The authors declare no competing interests.

Reprints and permission information is available online at http://npg.nature.com/reprintsandpermissions/

Publisher's note: Springer Nature remains neutral with regard to jurisdictional claims in published maps and institutional affiliations.